Earth Planet. Sci. Lett. 693 (2026) 120298

Contents lists available at ScienceDirect

Earth and Planetary Science Letters

journal homepage: www.elsevier.com/locate/epsl

West Antarctic subglacial geology distinguished by Pb isotopes and Rb–Sr ages in ice-rafted feldspars

Thomas Arney [a,b,*], Claus-Dieter Hillenbrand [b], Thomas M. Belgrano [c], J. Andy Milton [a], Christine S. Siddoway [d], Gavin L. Foster [a], Paul A. Wilson [a], Julia S. Wellner [e], Steve M. Bohaty [f]

[a] *School of Ocean and Earth Science, University of Southampton, Waterfront Campus, National Oceanography Centre, Southampton, UK*
[b] *British Antarctic Survey, High Cross, Madingley Road, Cambridge, UK*
[c] *UCD School of Earth Sciences, University College Dublin, Belfield, Dublin, Ireland*
[d] *Geology Department, Colorado College, Colorado Springs, CO, USA*
[e] *Department of Earth and Atmospheric Sciences, University of Houston, Houston, TX, USA*
[f] *Institute of Earth Sciences, Heidelberg University, Heidelberg, Germany*

A R T I C L E I N F O

Editor: Dr Andrew Zuza

Keywords:
Pb isotopes
Rb-Sr geochronology
Feldspar
Ice-rafted debris
West Antarctica
Inverse provenance

A B S T R A C T

Provenance data from sediment delivered to the marine environment by icebergs can trace past ice sheet dynamics and help constrain the ice sheet models used in sea level projections. This approach requires an interpretative framework, but in Antarctica, blanketing ice sheets hinder knowledge of upstream geology. Here, we tackle this problem by presenting a coupled laser ablation–based Pb isotope and Rb–Sr age study of ice-rafted feldspar grains from shelf sediments along West Antarctica's Pacific margin. We identify five distinct clusters in Pb isotope composition, each associated with Rb–Sr age clusters interpreted as West Antarctic magmatic episodes. One cluster suggests granitoids recently identified in geophysical data from the Thwaites Glacier bed may be Ross orogen plutons in a rifted block of Transantarctic Mountains crust. A Middle Jurassic cluster fringing the Thurston Island crustal block reflects Chon Aike magmatism, and a cluster restricted to western Marie Byrd Land points to extensive subglacial exposure of Carboniferous anatectic granites in the Ford Ranges. These Pb isotope groups can be used as tracers to infer past ice extent and erosional dynamics of glaciers in the Amundsen Sea Embayment, including the Thwaites and Pine Island glaciers. Our approach provides a powerful and high-throughput tool for studying detrital provenance in West Antarctica and could be generalized for use in other inverse provenance studies around Antarctica and beyond.

1. Introduction

The West Antarctic Ice Sheet (WAIS) plays a critical role in projections of global sea level rise because of the vulnerability of its marine-based grounding zones to ocean-induced melting. Projections can be improved by evaluating ice sheet models using data that document ice extent under different climate states (e.g., Halberstadt et al., 2024).

Provenance studies of material deposited by icebergs (ice-rafted debris: IRD) can provide such evidence, but this forward modelling approach requires a good understanding of hinterland geology. In Antarctica, extensive ice cover means the geology is less precisely mapped than in most other regions. Subglacial bedrock characteristics are mostly inferred from interpolation of geophysical data between rare (often isolated) outcrops. Powerful constraints on the upstream geology can also be gained from geochemical and mineralogical analysis of IRD deposited near the present-day ice sheet terminus, derived from otherwise inaccessible regions. This inverse provenance approach allows tectonic reconstructions (Flowerdew et al., 2013a; Mulder et al., 2019) and enables later forward-modelling studies which can assign approximate sources to pre-Holocene IRD in offshore records (Bailey et al., 2022; Williams et al., 2010).

The coarse (>150 µm) fraction of West Antarctic sediments contains predominantly quartz and feldspar grains because the region has hosted a continental arc, with intermediate to felsic magmatism, for the majority of the last ∼500 Ma. Using these abundant feldspar grains as provenance tracers therefore requires a smaller sediment sample for

* Corresponding author.
E-mail address: t.arney@soton.ac.uk (T. Arney).

https://doi.org/10.1016/j.epsl.2026.120298
Received 23 July 2026; Received in revised form 17 August 2026; Accepted 18 August 2026
Available online 29 August 2026

analysis compared to accessory phases such as zircon. Small sample sizes are particularly necessary at very remote locations (e.g., the Amundsen Sea) where dense annual sea-ice cover often hinders sample collection. Using coarse K-feldspar (Kfs) grains does, however, introduce a bias away from mafic lithologies and lithologies absent from the sand fraction, such as fine-grained or friable rocks. A combination of tracers reflecting different and complementary aspects of the hinterland geology can be analysed to counter the biases of any single tracer – for example, Sr and Nd isotopic composition of fine-grained detritus (Simões Pereira et al., 2018), U–Pb dating of coarse detrital zircons (Licht et al., 2014; Marschalek et al., 2025), $^{40}Ar/^{39}Ar$ dating of hornblende and mica grains (Bailey et al., 2022; Simões Pereira et al., 2018), apatite thermochronology (Lindow et al., 2016), and clay mineral assemblages (Ehrmann et al., 2011). Geochronological tracers are particularly useful since the results can be directly compared (with caveats) to diverse onshore age data.

Recent advances in laser-ablation reaction-cell tandem mass spectrometry (LA–ICP–MS/MS; Hogmalm et al., 2017) allow many Kfs grains to be dated by in situ Rb–Sr geochronology, complementing well-established LA–multi-collector (MC)–ICP–MS Pb isotopic feldspar provenance methods (Tyrrell et al., 2006). Analysis by these two methods yields a powerful coupled tracer for large populations of individual grains (Neofitu et al., 2024).

Existing Pb isotope data of feldspars from West Antarctica form a tight cluster compared to East Antarctic data (Fig. 1). Feldspar grains with a West Antarctic origin can therefore be readily distinguished from East Antarctic grains in marine sediments (Flowerdew et al., 2012). However, existing West Antarctic bedrock data, restricted to ice-free outcrops, are sparse and therefore may not reflect the full variability of Pb isotopic compositions within West Antarctica. In contrast, ice-rafted feldspars likely originate from multiple subglacial sources with a wider range of Pb isotope compositions. Hundreds of grains must be analysed to build robust conclusions, which is now possible through high-throughput laser ablation methods.

Here, we perform an exploratory Pb isotope analysis of individual ice-rafted feldspar grains from ice-proximal marine sediments, in combination with in situ Rb–Sr dating of a subset of the same grains. We use an inverse provenance approach based on clustering to interpret our Pb isotope data, supported and validated by comparing the linked geochronological results to known onshore data. We interpret these results in the context of the known onshore geology and tectonic history of the region and infer possible sources for each cluster.

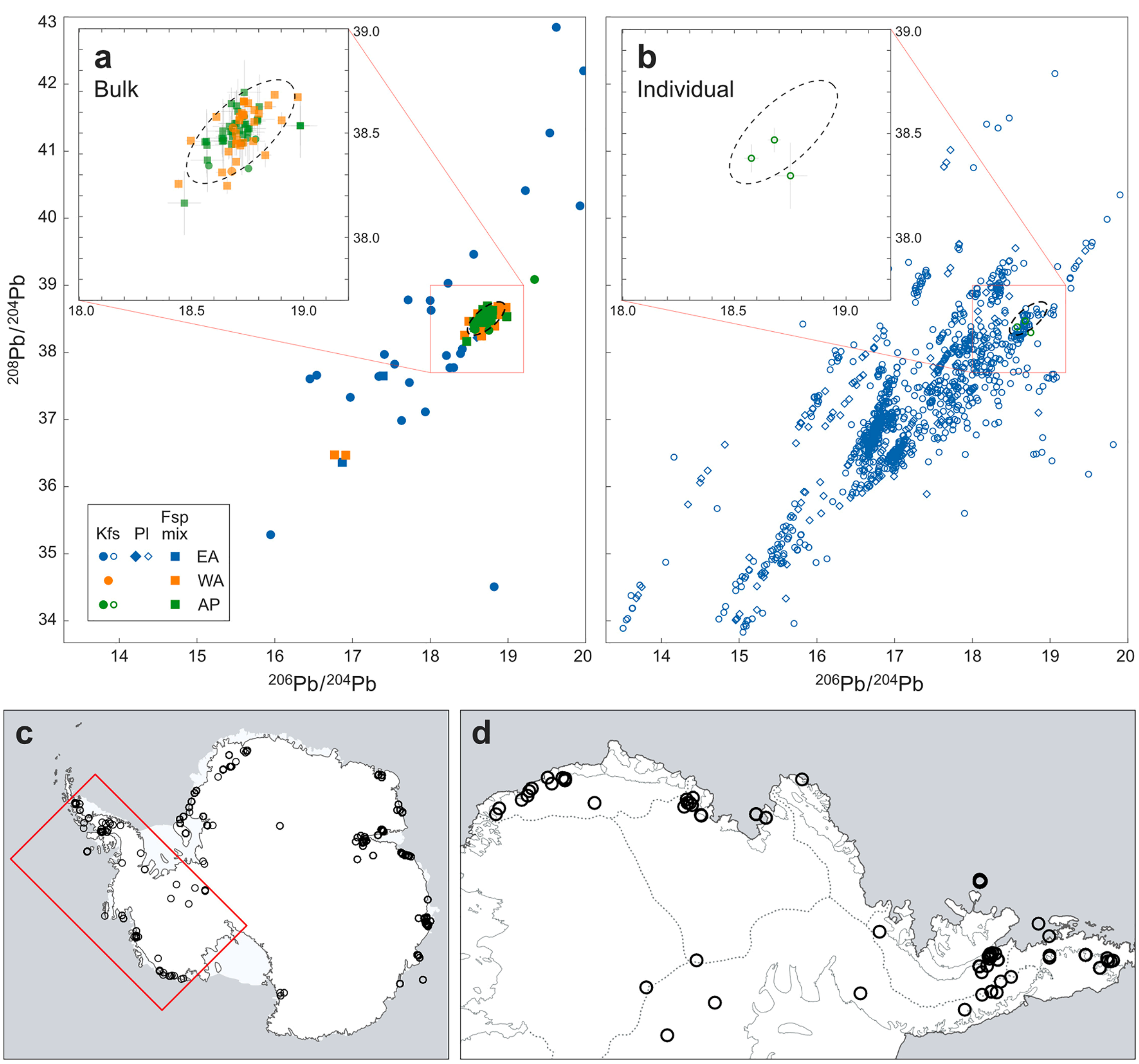

Fig. 1. Compiled Pb isotope data in feldspars from Antarctic bedrock and sediments. **a**, Bedrock $^{206}Pb/^{204}Pb$ versus $^{208}Pb/^{204}Pb$ measured in bulk mineral separates of K-feldspar (Kfs), plagioclase (Pl), or undifferentiated mixtures (Fsp mix). **b**, Pb isotopes in individual K-feldspar and plagioclase grains from detrital sediments and sedimentary rocks. **Insets** in (a) and (b) show a detailed view of West Antarctic (WA) (including Antarctic Peninsula, AP) data, and excluding East Antarctic (EA) data. Dashed ellipses show the 95% confidence interval of a bivariate normal distribution fitted to the West Antarctic data. **c**, sample locations for the data shown in (a) and (b). **d**, detailed view of West Antarctic sample locations. Compiled data with sources are given in Table S1.

1.1. Geological setting

West Antarctic crust predominantly consists of sedimentary accretionary prisms and intermediate to felsic magmatic arcs formed along the convergent margin of Gondwana from the early Paleozoic (~500 Ma) to the Cretaceous (~100 Ma). The Antarctic Peninsula and Thurston Island crustal block (TICB) experienced almost continuous magmatism punctuated by periodic flare-ups through the Paleozoic and Mesozoic (Riley et al., 2018), while Marie Byrd Land (MBL) underwent two major magmatic episodes in Devonian-Carboniferous and Cretaceous times (Jordan et al., 2020). Spatial relationships among tectonic blocks constituting West Antarctica today (Fig. 2) were much the same in Gondwana, except that the subcontinent of Zealandia lay outboard of (proto-) MBL (Mortimer et al., 2019), and that tectonic blocks now forming Patagonia possibly originated from the early Paleozoic convergent margin (González et al., 2018).

The tectonic histories of the Antarctic Peninsula/TICB and MBL diverged in the Jurassic. The former records ongoing magmatism, whereas MBL, situated inboard of the Gondwana margin arc that passed through Zealandia, lacks any post-Carboniferous magmatism until the appearance of ~125–90 Ma granites. These plutons intruded during the broad intra-continental extension across MBL-southern Zealandia (Jordan et al., 2020; Siddoway et al., 2004), which initiated the West Antarctic Rift System. Subduction ceased by ~105 Ma (Luyendyk, 1995) and was followed by breakup between Zealandia and MBL by ~84 Ma (Mortimer et al., 2019), leading to the development of the West Antarctic passive margin. Meanwhile along the (proto-)Pacific margin of the Antarctic Peninsula, plate subduction halted progressively from south to north. Since the Miocene, dispersed mafic alkalic volcanism has occurred across MBL and the West Antarctic Rift System.

2. Materials and methods

Surface sediment samples from 25 core sites on the West Antarctic continental shelf (Fig. 3, Table S2) were selected to cover various drainage sectors of the WAIS and Antarctic Peninsula Ice Sheet. Samples typically spanned the top ~4 cm of each core, but sampling down to 10–17 cm was required for some heavily sampled or very fine-grained cores (see Table S2). At all sites, however, the analysed sediments most likely have a (Late) Holocene age, given the typical thickness of Holocene sediments in the study area (e.g., Larter et al., 2014). The samples should therefore reflect modern erosional, transport, and depositional patterns, with coarse detrital grains supplied by iceberg-rafting or (rarely) ice-shelf rafting. Sea-ice rafting can be discounted given the over-deepened continental shelf.

A total of 1670 coarse (>150 µm; see Table S2) detrital mineral grains were picked from the washed sediment samples, mounted in epoxy, ground, and polished. To optimize sample throughput, the number of grain mounts was reduced by not mounting the entirety of each size fraction. Instead, ~50–100 grains were picked from each sample – many more than eventually analysed – to mitigate any bias. The grain mounts were screened using a Leo 1450VP variable pressure scanning electron microscope with an Oxford Instruments X-act 10 mm^2 area energy dispersive spectrometer (SEM–EDS). Relative major element abundances were determined using AZtec v5.0 software. Laser spots were set using the SEM–EDS images in TACtool (https://doi.org/10.5281/zenodo.11236874).

Lead isotope ratios were measured in 643 Kfs grains, Rb–Sr isotopes in 336 of the same grains, and $^{87}Sr/^{86}Sr$ was additionally measured in 138 plagioclase grains. All isotopic analyses were conducted at the Centre for Earth Research and Analysis, Southampton (CERAS; University of Southampton, UK) using one of two 193 nm UV excimer lasers: either an Elemental Scientific Lasers NWR193 equipped with a TwoVol2 sample chamber or a Teledyne Iridia laser with a Cobalt sample chamber. Helium (700–1000 ml.min^{-1}) was used as the sample carrier gas, with a post-cell nitrogen addition (2–8 ml.min^{-1}) for enhanced sensitivity. Instruments were tuned in each session to maximize sensitivity and minimize oxide production while ablating NIST 612.

2.1. Pb isotope measurements

For Pb isotopic analysis, the NWR193 laser was coupled to a Thermo Scientific Neptune Plus multi-collector ICP–MS (LA–MC–ICP–MS) equipped with a Ni X skimmer cone and a Ni Jet sampler cone. A laser spot size of 150 µm with ~5.5 J.cm^{-2} fluence and repetition rate of 10 Hz was chosen to maximize ion yield. Ablations lasted 60 s with a 60 s washout period. Integrations for each analysis were trimmed to 55.5 s and visually screened in iolite 4 (Paton et al., 2011) to omit inclusions and any cycles after grains had been ablated through. Bracketing analyses of NIST 610 every 10 sample spots were used for primary

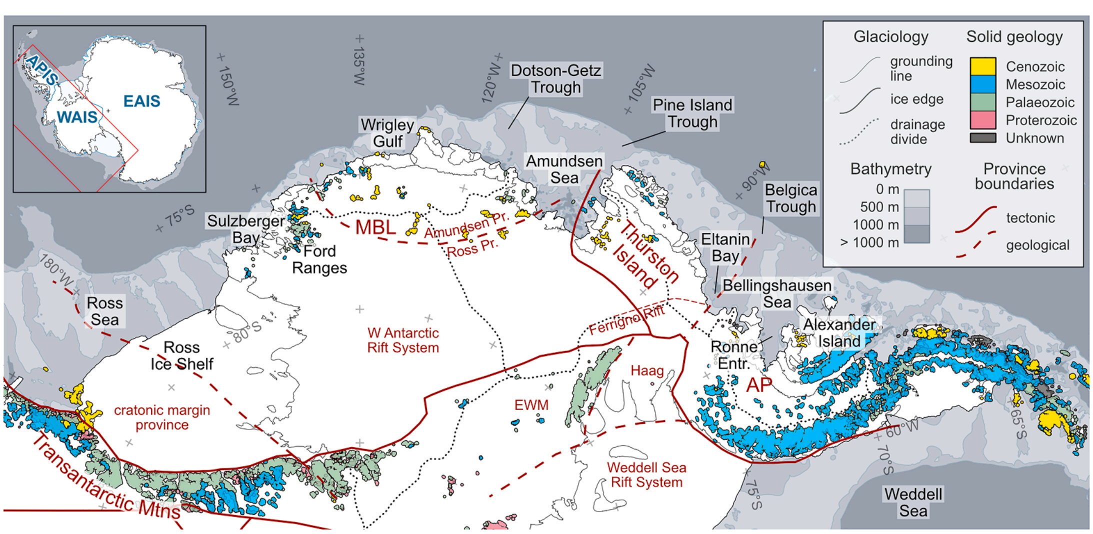

Fig. 2. Geology of West Antarctica and neighbouring areas based on the outcrop age compilation of Cox et al. (2023) (outcrop areas expanded for clarity), colour coded by geological era. Geotectonic provinces and sub-provinces from Jordan et al. (2020). Bathymetry from the International Bathymetric Chart of the Southern Ocean (Arndt et al., 2013). MBL: Marie Byrd Land; AP: Antarctic Peninsula; EWM: Ellsworth-Whitmore Mountains. **Inset**: W(E)AIS: West (East) Antarctic Ice Sheet; APIS: Antarctic Peninsula Ice Sheet.

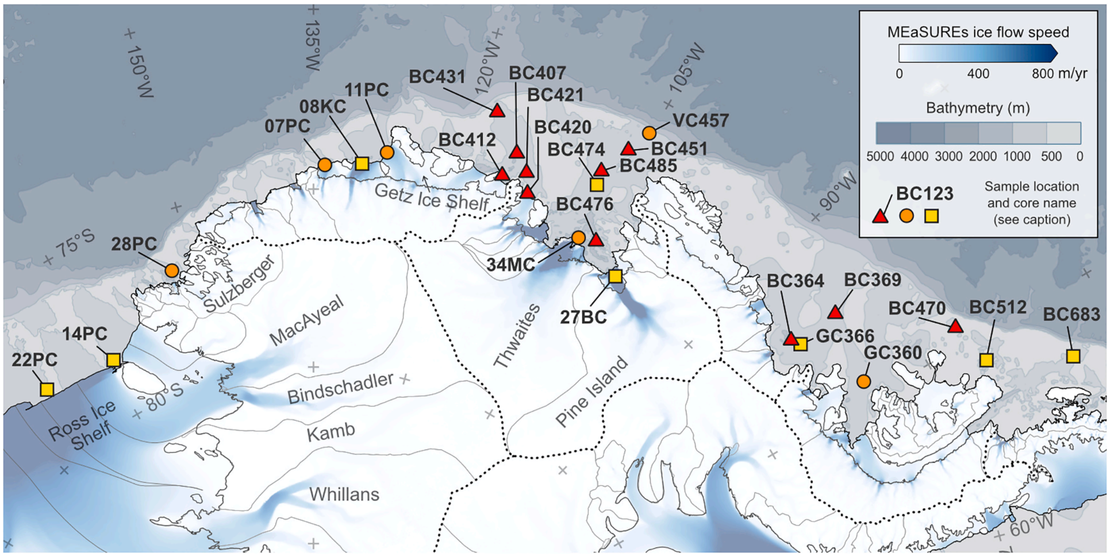

Fig. 3. Map of the surface sediment sample sites used in this study. Labels refer to core names: see Table S2 for details. Marker shapes show relationships between sites in this study and those in Simões Pereira et al. (2018): triangles: identical, circles: within 20 km of an equivalent, squares: no equivalent. Also shown are glacial drainage basins (grey lines: boundaries; dotted lines: ice divides) and 'Making Earth System Data Records for Use in Research Environments' (MEaSUREs) ice flow speed (Mouginot et al., 2017). PC: piston core, BC: box core, GC: gravity core, KC: kasten core, VC: vibrocore.

calibration, correcting for system mass bias and drift. Reference materials NIST 612 and USGS basalt glass BCR-2G were used to assess measurement quality (see Table S4).

The isotopes ^{202}Hg, ^{204}Pb, ^{206}Pb, ^{207}Pb, ^{208}Pb were monitored on Faraday detectors, with 10^{11} Ω amplifiers assigned to ^{206}Pb, ^{207}Pb, and ^{208}Pb, and 10^{12} Ω amplifiers to ^{202}Hg and ^{204}Pb. Isobaric interference of ^{204}Hg on ^{204}Pb was corrected by assuming a ^{204}Hg/^{202}Hg ratio of 0.2301 (Laeter et al., 2003).

Low natural abundance of ^{204}Pb (~1.4%) results in undesirably low-precision ^{204}Pb-normalized ratios when measured via this method. ^{206}Pb or ^{207}Pb-normalized ratios (with precision an order of magnitude better) are more suitable for LA–MC–ICP–MS detrital studies. The half-life of the decay from ^{235}U to ^{207}Pb is 704 Myr compared to 4.463 Gyr for ^{238}U to ^{206}Pb. With more half-lives elapsed and the low natural abundance of precursor ^{235}U, ^{207}Pb is less variable in young (<500 Ma) rocks than ^{206}Pb. We therefore use ^{207}Pb-normalization in our Pb isotope analyses and include ^{204}Pb-normalized ratios for reference and evaluation of crustal evolution.

For all ^{204}Pb-normalized ratios, NIST 612 precision was ≤1.2% 2RSD (two relative standard deviations) and accuracy was within 0.25%. BCR-2G precision was ~2.7% and accuracy was within ~0.01–0.02%. Precision and accuracy were better for all ^{207}Pb-normalized ratios, at <0.2% and <0.02% (NIST 612) and ~0.35% and <0.09% (BCR-2G) respectively (Table S4). Measurements of unknowns with two standard error (2SE) uncertainties >0.003 (^{206}Pb/^{207}Pb) or >0.004 (^{208}Pb/^{207}Pb) – i.e., worse than ~0.2% 2RSE – were discarded (3.4% of data).

2.2. Rb–Sr geochronology

Detrital feldspar Rb–Sr geochronological analysis took place over two sessions. The laser was coupled to an Agilent 8900 triple-quadrupole inductively coupled plasma tandem mass spectrometer (LA–ICP–MS/MS). Ablation parameters were tuned for each session such that both Rb and Sr were measured in pulse mode for all analyses. The NWR193 laser was used in the first session (240507), and circular laser spots of 90 µm diameter at ~3 J.cm^{-2} fluence and a repetition rate of 5 Hz were used for all reference materials and unknowns, apart from a subset of plagioclase grains, identified by SEM–EDS, which were ablated with a 150 µm spot to constrain the range in possible initial Sr values. In the second session (251017), the Iridia laser was used, and parameters were adjusted to ~1.3 J.cm^{-2} fluence and a repetition rate of 15 Hz, with spot sizes of 70 µm (Kfs) and 160 µm (plagioclase) to account for additional reference materials (see below). All ablations lasted 30 s with a 30 s washout time. Following Hogmalm et al. (2017), SF_6 premixed at a 10:90 volume ratio with He at a flow rate of 1 ml.min^{-1} and H_2 at 1 ml. min^{-1} were used as reaction gasses for shifting Sr isotopes to SrF^+ masses for measurement free from isobaric ^{87}Rb interference, and to eliminate ^{40}Ar tail interference on ^{39}K for more accurate major element determination.

Data were first processed in iolite 4 using an SF_6-adapted version of the Redaa et al. (2021) Rb–Sr data reduction scheme. Intensities for ^{87}Rb were calculated from ^{85}Rb, assuming a natural ^{87}Rb/^{85}Rb ratio of 0.38562. The gas background was defined using the last ~23 s of each washout period. The signal for each analysis was trimmed to 25 s and then visually screened in iolite for inclusions. Following Glorie et al. (2024), NIST 610 was used as the primary reference material for initial isotope ratio normalization and drift correction, using a standard-sample bracketing protocol. Measurement errors are reported with 2SE uncertainties.

Rb/Sr fractionation during ablation necessitates a second step of matrix-matched ^{87}Rb/^{86}Sr calibration (Glorie et al., 2024; Hogmalm et al., 2017); however, suitable internationally distributed materials are not presently available. Calibration with a NIST SRM607a K-feldspar nano-powder pellet produced inaccurate results, confirming previous work (Glorie et al., 2024). We instead used in-house orthoclase-bearing samples from the Mountsorrel Granodiorite (Leicestershire, England), the Dartmoor Granite (Devon, England), and the Mourne Mountains (G2 granite, County Down, Northern Ireland), the latter two of which have been characterized for Rb–Sr reference material potential in a forthcoming study (Corella Santa Cruz et al. in prep).

The Mountsorrel Granodiorite has a whole-rock Rb–Sr isochron age of 432 ± 16 Ma, recalculated after Cribb (1975), and an unabraded zircon U–Pb discordant upper intercept age of 452 ± 10 Ma (Noble et al., 1993). An independent biotite Rb–Sr age of 430 ± 8 Ma (Fig. S1) is indistinguishable from the Cribb (1975) whole-rock age.

A sample (HG-1) of 'poorly megacrystic' Dartmoor Granite (terminology of Darbyshire and Shepherd, 1985, and references therein) from Haytor West Quarry, Dartmoor, was sourced from the University of

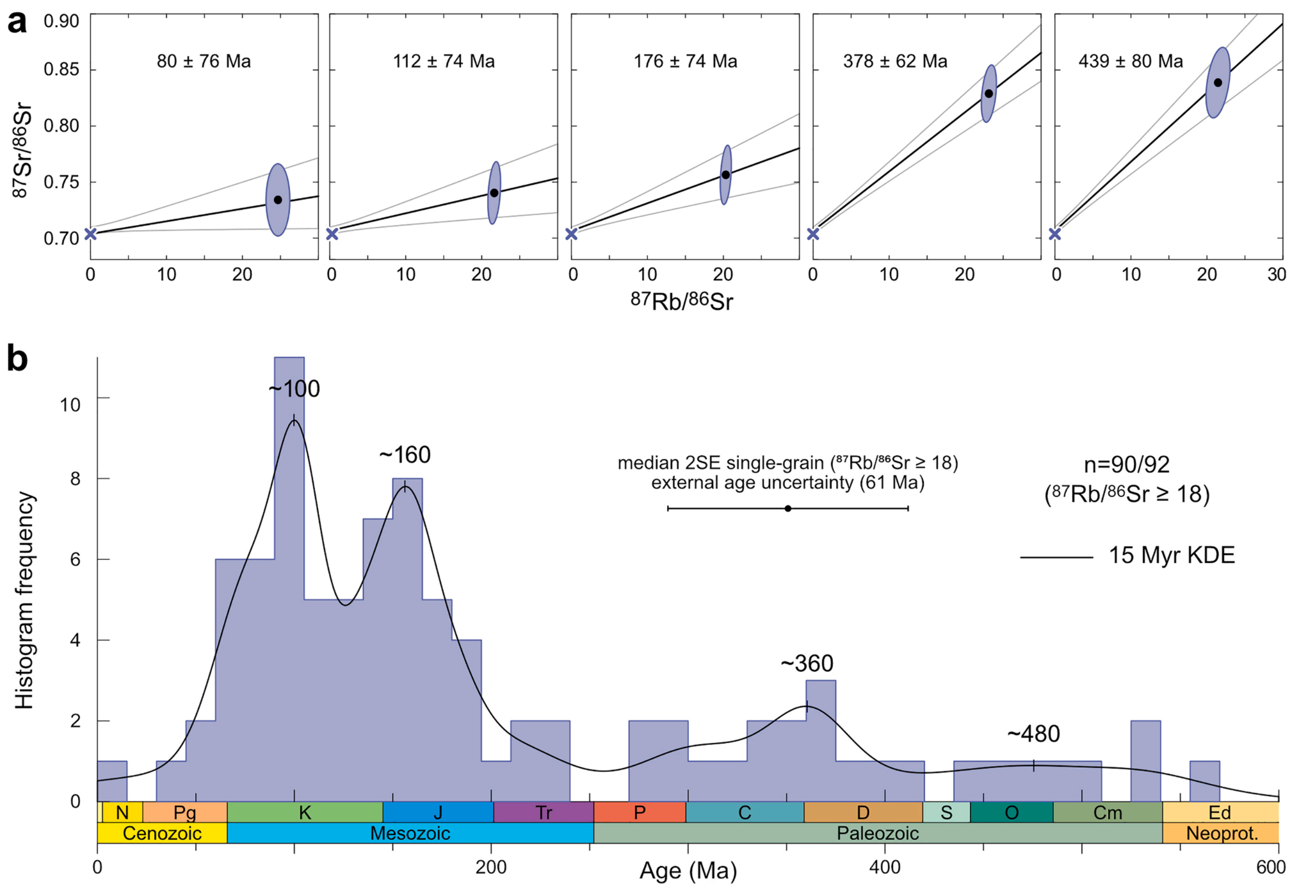

Fig. 4. Rb–Sr K-feldspar (Kfs) detrital geochronology. **a**, Two-point isochrons of five Kfs grains (measured spots with 2SE ellipses), anchored to a fixed initial $^{87}Sr/^{86}Sr$ (purple crosses), illustrating the age calculation method for all our detrital grains. **b**, Histogram and kernel density estimate (KDE) of detrital grain ages (filtered to $^{87}Rb/^{86}Sr \geq 18$) as calculated in (a). KDE (adaptive) bandwidth and histogram bin widths are 15 Myr. Peaks on the KDE are labelled with approximate ages (rounded to 10 Ma).

Liverpool teaching collection (via UKGE Ltd.). An isotope dilution mineral separate isochron of similar granite from the same Haytor West Quarry yields a reference age of 283 ± 3 Ma (recalculated after Darbyshire and Shepherd, 1985).

Sample BB-G2 consists of orthoclase crystals picked from a miarolitic cavity in Mourne granite 'G2' (Corella Santa Cruz et al., in prep), with a (recalculated) whole-rock Rb–Sr age of 56.81 ± 0.41 Ma (Gibson et al., 1987).

Plagioclase and Kfs in HG-1 were measured in both sessions and used for Rb/Sr matrix correction. The initial Sr isotope ratio ($^{87}Sr/^{86}Sr_i$) of Darbyshire and Shepherd (1985) was used to constrain a preliminary NIST-calibrated Kfs Rb–Sr age calculated in IsoplotR (Vermeesch, 2018). The offset from the recalculated 283 ± 3 Ma reference age was then used for calculating $^{87}Rb/^{86}Sr$ correction factors for all unknowns within that session.

Accuracy was assessed through measurement of Mountsorrel feldspars in both sessions and the Mourne feldspar in the second session. Isochrons constructed with $^{87}Sr/^{86}Sr_i$ fixed to that calculated by Cribb (1975) yield ages of 404 ± 27 Ma (2SE external uncertainty; mean square of the weighted deviates (MSWD) = 1.01) and 420 ± 37 Ma (MSWD = 1.48), which are within uncertainty of the expected 432 ± 16 Ma age, albeit relatively imprecisely due to moderate $^{87}Rb/^{86}Sr$ ratios (Fig. S3a and c). In session two, an HG-1 calibrated age of 55.7 ± 5.3 Ma (MSWD = 0.88) was calculated for BB-G2 from an isochron fixed through the $^{87}Sr/^{86}Sr_i$ of Gibson et al. (1987) (Fig. S3b). Keeping ^{85}Rb counts in pulse mode for high Rb BB-G2 necessitated the change in laser parameters for session two.

2.3. Elemental concentrations

Concentrations of K, Na, Ca, Pb, Rb, and Sr were measured alongside Rb–Sr isotopes. Unknowns were calibrated with bracketing analyses of NIST 610, using Si as an internal standard. An approximated value of 60 wt% SiO_2 was used for all unknown feldspars. Reference material USGS BCR-2G was used to assess measurement quality: precision was ~10% 2RSD and accuracy for all elements was within 10%, except Pb (11%) and K (17%) (Table S5).

2.4. Data analysis

Lead isotope ratio cluster analysis was conducted with the scikit-learn Python library in two steps. First, a training dataset was prepared by removing the less precise half of the data, followed by normalization and scaling. The OPTICS clustering algorithm (Ankerst et al., 1999) was used to remove data points from very low-density areas (i.e., outliers). A Gaussian Mixture Model (GMM) was then fitted to the remaining data. In the second step, the trained GMM was used to classify the unfiltered dataset. Any data points with a log-likelihood value below a threshold containing 99.9% of the GMM were left unclassified (=27% of data). This composite method avoids the inability of GMMs to ignore outliers during fitting while retaining their ability both to account for overlapping clusters and to classify new data.

Detrital Rb–Sr ages were calculated in IsoplotR in two ways. Individual single-spot ages were calculated using two-point isochrons between the analysed spots and the weighted mean ± 2SE $^{87}Sr/^{86}Sr_i$ of plagioclase analyses (Fig. 4a) (cf. Neofitu et al., 2024). Ages for Pb isotope-clustered groups were calculated by conventional multi-point isochrons without $^{87}Sr/^{86}Sr_i$ anchoring. The ages obtained are interpreted as magmatic crystallization ages, except where otherwise noted. Following Rösel and Zack (2022), systematic uncertainties were added in quadrature to the internal 2SE uncertainties for all calculated ages. Plagioclase analyses were screened for $^{87}Rb/^{86}Sr$ >0.3 or >0.1 molar K/(K+Na+Ca) (Fig. S4b), leaving 73 grains with a weighted mean $^{87}Sr/^{86}Sr_i = 0.7066 \pm 0.0017$ used for all single-spot isochron calculations.

All 332 grains which have coupled Pb and Rb–Sr isotope data are included in our multi-point isochron analyses. Kernel Density Estimates (KDEs) use single-spot grain ages, some of which are relatively imprecise. Filtering directly on age uncertainty would bias the dataset toward older, more radiogenic grains. Since age uncertainty is inversely related to the $^{87}Rb/^{86}Sr$ ratio, we instead limit KDE analyses to grains with $^{87}Rb/^{86}Sr$ >18 (28% of measured grains).

3. Results

A KDE fitted to the filtered Rb–Sr ages reveals a broad Mesozoic peak and a long Paleozoic tail, the former comprising middle Cretaceous (~100 Ma) and Jurassic (~160 Ma) components (Fig. 4b). Paleozoic grains form a peak of Devonian–Carboniferous (~360 Ma) age and a Cambrian–Ordovician plateau with a central age of ~480 Ma.

The major component in the Pb data (>80%) falls within the range of existing West Antarctic bedrock data (Fig. 1a), but a small proportion (~10%) of the data lies outside the bedrock data range, in the less

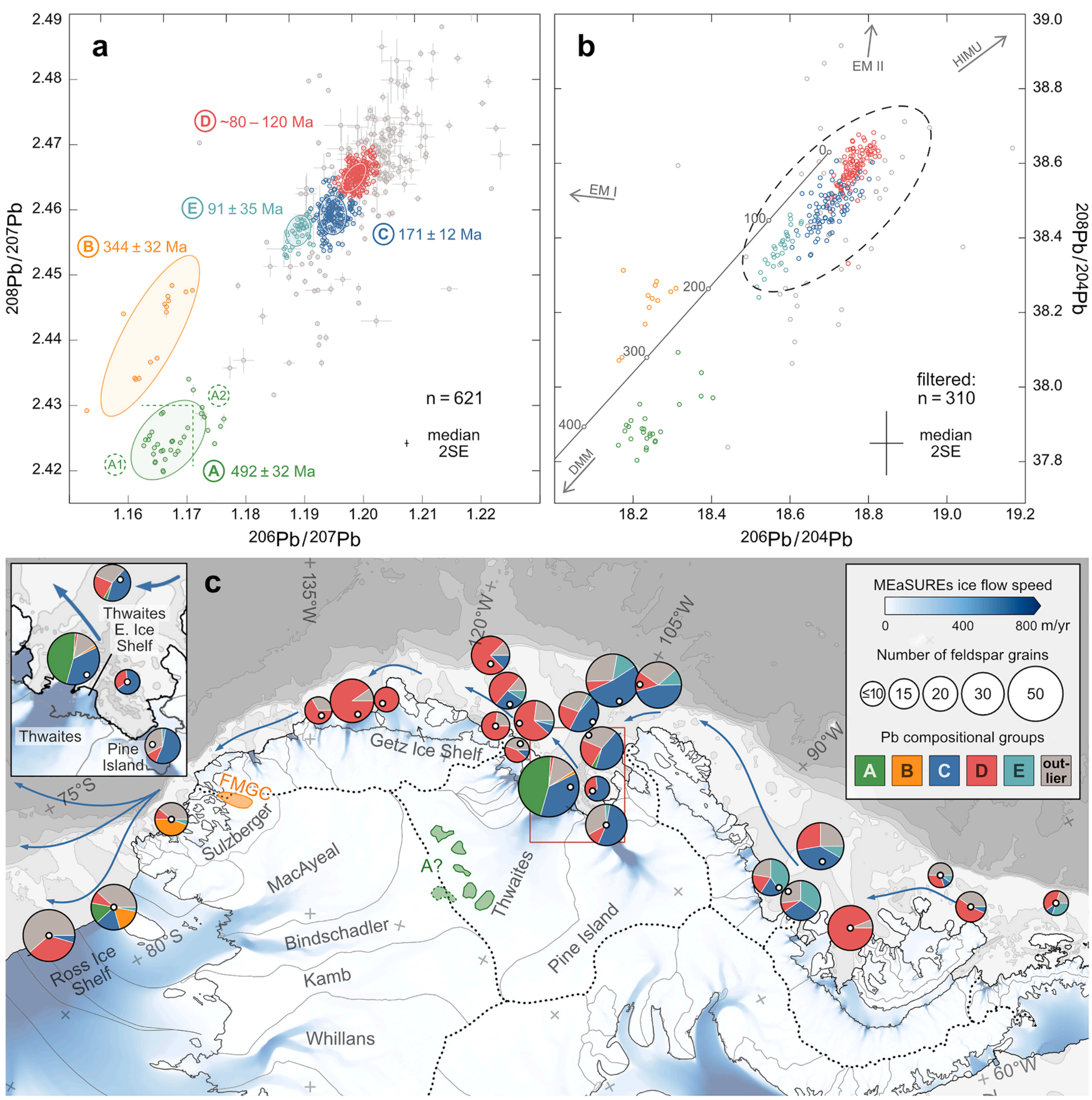

Fig. 5. Clustering of Pb isotope ratios in ice-rafted K-feldspar grains. **a**, $^{206}Pb/^{207}Pb$ versus $^{208}Pb/^{207}Pb$ (i.e., ^{207}Pb-normalized; n = 621, including 13 outliers outside the plot area). Ellipses represent the 95% confidence interval of modelled Gaussian distributions of each group (A to E), with associated Rb–Sr isochron ages (±2SE external uncertainty). Error bars show 2SE analytical uncertainty. **b**, A subset of $^{206}Pb/^{204}Pb$ versus $^{208}Pb/^{204}Pb$ (i.e., ^{204}Pb-normalized) data, coloured by the clusters in (a). For clarity, error bars are omitted and data is filtered (n = 310) to show the more precise half of the data. The median 2SE analytical uncertainty for the unfiltered dataset is shown for reference. The two-stage terrestrial Pb evolution curve of Stacey and Kramers (1975) and mantle end members are plotted for reference. Axis scales and dashed ellipse showing the range of existing Antarctic Pb-in-feldspar data are the same as Fig. 1a (inset) for comparison. **c**, Distribution of Pb clusters from (a) by sample location. Pie charts show the proportion of grains falling in each group, while the size of each pie chart is proportional to the number of grains analysed. Iceberg drift is schematically represented by blue arrows (e.g., Rackow et al., 2017). 'A?' shows the approximate hypothesised position of the source of Group A grains (see text). FMGC: Fosdick Migmatite-Granite Complex. **Inset**: detailed view of inner Pine Island Bay.

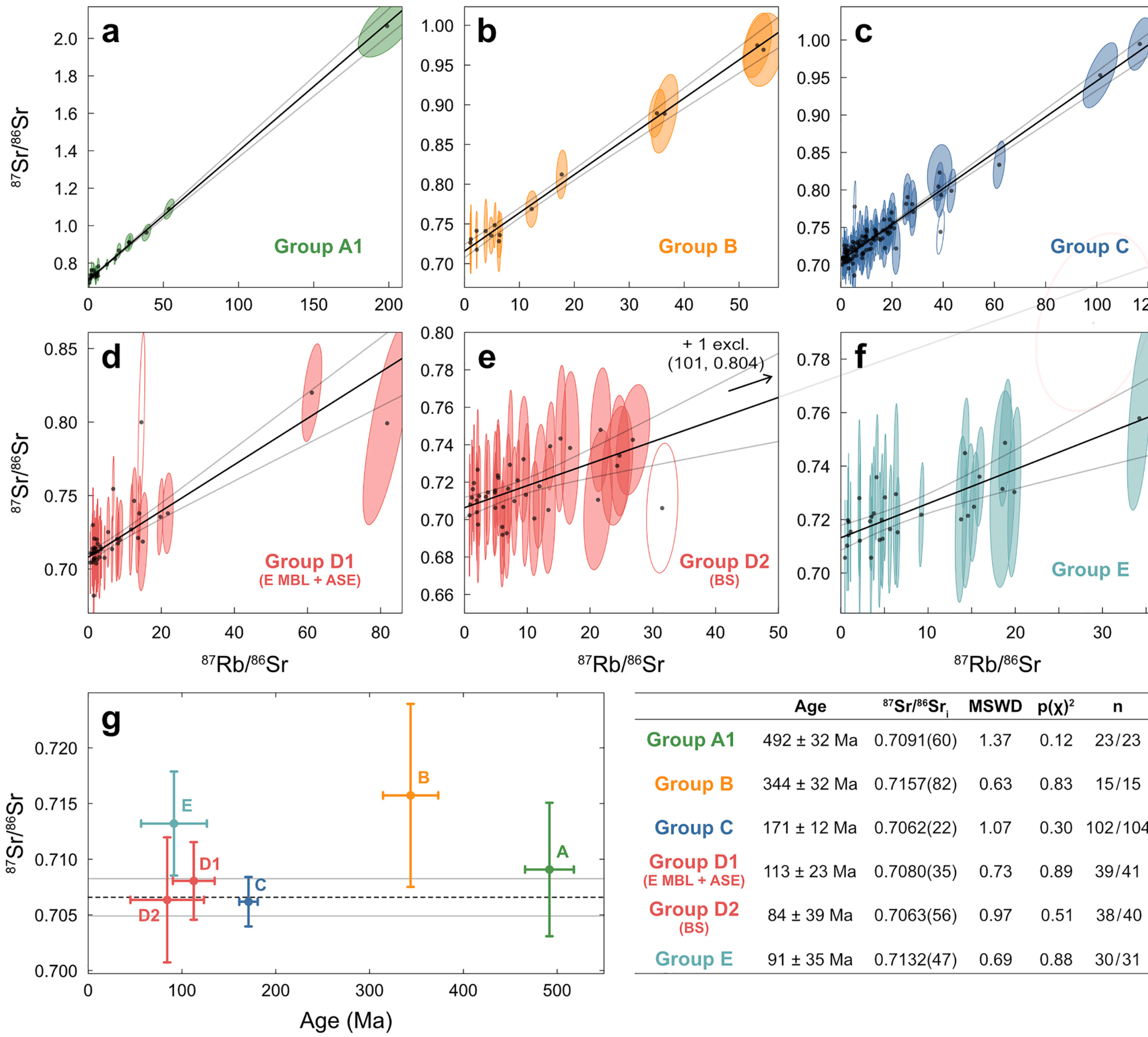

	Age	$^{87}Sr/^{86}Sr_i$	MSWD	$p(\chi)^2$	n
Group A1	492 ± 32 Ma	0.7091(60)	1.37	0.12	23/23
Group B	344 ± 32 Ma	0.7157(82)	0.63	0.83	15/15
Group C	171 ± 12 Ma	0.7062(22)	1.07	0.30	102/104
Group D1 (E MBL + ASE)	113 ± 23 Ma	0.7080(35)	0.73	0.89	39/41
Group D2 (BS)	84 ± 39 Ma	0.7063(56)	0.97	0.51	38/40
Group E	91 ± 35 Ma	0.7132(47)	0.69	0.88	30/31

Fig. 6. Isochron-derived Rb–Sr ages and initial $^{87}Sr/^{86}Sr$ for the Pb groups. **a**–**f**, Isochrons constructed using data grouped by the Pb clustering. Colours and groups correspond to those in Fig. 5. Isochrons (black lines) are shown with 95% confidence intervals (grey area). Ellipses show the analytical error for each data point. A small number are excluded from the fit (empty ellipses) if they are clear outliers or their individual inclusion significantly affects the age. One spot at $^{87}Rb/^{86}Sr = 101$, shown semi-transparent outside the plot area, and another at 31 are excluded from the Group D2 fit; including them individually yield ages of 64 ± 36 Ma and 74 ± 23 Ma. n = number of data points included out of the total in the group. MSWD = mean square of the weighted deviates; $p(\chi^2)$ = chi-squared p-value for the linear fit. **g**, Comparison of $^{87}Sr/^{86}Sr_i$ and age for each group, derived from the isochron regressions. Also shown (dashed line) is the regional weighted mean ± 2SE $^{87}Sr/^{86}Sr$ of plagioclase grains from the same samples as the Kfs grains, used for the detrital age calculations. All errors quoted are 2SE.

radiogenic direction of the ^{204}Pb-normalized plot (Fig. 5).

The internal variation observed within the major Pb isotope component (Fig. 5a, Fig. S5) and in the Mesozoic Rb–Sr data suggests the existence of smaller sub-components. Our clustering analysis yielded five clusters in the Pb isotopic data, which we label Groups A to E. The same groups are distinguishable in similar relative positions when plotted using ^{204}Pb-normalized ratios (Fig. 5b).

The single-grain coupled-measurement approach allows us to assess the Rb–Sr ages corresponding to each Pb isotope compositional group. All five groups have a detrital Kfs age distribution dominated by a single peak (Fig. S6). We therefore fitted isochrons to the Rb–Sr data from these groups, without $^{87}Sr/^{86}Sr_i$ assumptions, to arrive at more precise Rb–Sr ages than is possible from single grain analyses.

4. Discussion

Group A feldspars occur nearly exclusively at two sites: 34MC (Thwaites Eastern Ice Shelf) and 14PC (eastern Ross Ice Shelf), separated by ~1500 km and an ice-drainage divide (Fig. 5). Combining all Group A feldspar grains yields a slightly overdispersed errorchron of 486 ± 36 Ma (MSWD = 1.57), suggesting some geological diachroneity. Constructing Rb–Sr isochrons using only Group A grains from each site does not resolve the scatter, but restricting Group A to the main body of the cluster (henceforth Group A1 – i.e., retaining those grains with $^{206}Pb/^{207}Pb \leq 1.171$ and $^{208}Pb/^{207}Pb \leq 2.43$; Fig. 5a) yields a coherent isochron of 492 ± 32 Ma (MSWD = 1.37; Fig. 6a). Grains assigned to Group A1 are present in both samples 34MC (n = 22) and 14 PC (n = 2).

The small remainder of Group A (=Group A2, with grains from both sites) also forms an isochron, with a younger but very imprecise age that is within uncertainty of Group A1 (421 ± 85 Ma; n = 5; MSWD = 1.61). The very similar but non-identical signatures of Groups A1 and A2 may represent closely related but distinct sources.

The presence of Cambrian–Ordovician rocks under the Bindschadler Ice Stream (BIS), which flows into the eastern Ross Ice Shelf, has been noted previously: mineral grains of late Ross orogenic age (~520–475 Ma) were found in subglacial debris recovered from both upstream (Marschalek et al., 2024a) and downstream (Licht et al., 2014) areas. A few detrital zircon grains with similar U-Pb ages have recently also been observed in latest Holocene sediments from the Amundsen Sea Embayment (ASE) continental shelf, including a till sample from Thwaites Glacier, as well as Eocene and Mid-Cretaceous strata from this area, but they do not constitute a major age population in those samples (Marschalek et al., 2025).

Sandstone intervals within the voluminous turbidite succession eroded from the Ross orogen (Jordan et al., 2020) are a possible source for Group A feldspar. The Swanson Formation is kilometres thick in western MBL (Glen and Cooper, 2021) and is postulated to extend throughout MBL (Pankhurst et al., 1998; Spiegel et al., 2016). However, the youngest population of detrital zircons in this unit has a U-Pb age of 520–560 Ma (Adams et al., 2014), and metamorphism, dated by whole-rock Rb–Sr, occurred at ~444 Ma (Adams, 1986). Consequently, our Rb–Sr age of ~490 Ma for Group A Kfs grains precludes a source in the Swanson Formation. Additionally, grains in Group A have low analytical uncertainties and appear both angular and unaltered (Fig. S7). Primary erosion from crystalline bedrock rather than reworking from sedimentary units is therefore considered likely (Tyrrell et al., 2006).

Both our sample sites could have received material from ~490 Ma bedrock sources situated near the ice divide between Thwaites Glacier and BIS (Fig. 5), where negative gravity anomalies are mapped in a region of elevated topography and high bed roughness (Bingham and Siegert, 2009; Jordan et al., 2023). Although ice velocity is low in upstream areas, a rough bed induces high shear stress, a factor that promotes entrainment of bed material into the ice (Flowerdew et al., 2013b). The geophysical anomalies suggest the presence of felsic granitoids (Jordan et al., 2023), a potential source for Group A grains.

Two geological interpretations are consistent with the ~490 Ma age of Group A. The Ross orogeny in the Transantarctic Mountains (TAM) included plutonism with a post-tectonic peak at 495–490 Ma but with activity continuing until ~475 Ma (Goodge et al., 2024). Early Ordovician magmatism also occurred in the Famatinian arc, a part of the Northern Patagonia block restored to a position bordering MBL in palaeogeographic reconstructions (González et al., 2018; Riley et al., 2023). Either interpretation requires the existence of Paleozoic arc crust within the West Antarctic interior. Airborne gravity data provide evidence of broad basement 'ribbons' beneath the Ross Ice Shelf, attributed to multi-stage extension (Tankersley et al., 2022). Such a structure, a result of Paleozoic subduction retreat and extension (Glen and Cooper, 2021), could also underpin the West Antarctic interior, resulting in the transfer of faulted TAM crust into MBL. Alternatively, a fragment of the Ordovician arc may have been left behind during Mesozoic oblique subduction and dextral translation of the Famatinian belt along-strike to northern Patagonia (Rapela et al., 2018). Indirect evidence of the existence for arc crustal elements comes from sedimentary detritus shed into Permo-Triassic basins of the Antarctic Peninsula (Riley et al., 2023). Under either scenario, a concealed remnant of a Paleozoic margin arc would be present in MBL, providing a source for Group A grains.

Initial Sr isotopic ratios for TAM and Famatinian granites are very similar both to each other (~0.71; Goodge et al., 2012; Rapela et al., 2018) and to the unconstrained $^{87}Sr/^{86}Sr_i$ from the Group A1 isochron (0.7091 ± 0.0060, or ~0.711 if the isochron is fixed to 475 Ma; Fig. 6a), consistent with either hypothesis. The dominant 475 Ma age of Patagonian granitoids (Rapela et al., 2018) and the 495–490 Ma peak of post-tectonic Ross orogeny intrusions in the TAM (Goodge et al., 2024) are both within uncertainty of the 492 ± 32 Ma age of Group A1, though the latter is a closer match. Sparse data from the Famatinian arc of northwestern Argentina (Demartis et al., 2021) are a poor match to the Group A signature, and to our knowledge, no Pb isotopic data exist for the TAM. Without Pb isotopic data from both sources, neither hypothesis can be definitively discounted, but we consider a source originating in the TAM Ross orogen granitoids is more likely.

Group A grains are absent from more distal samples across the ASE shelf. This may result from dilution with detritus supplied from the eastern ASE coast, as observed in Nd isotope data of fine-grained sediment samples (Simões Pereira et al., 2018). Alternatively, Group A grains may not have been transported beyond the Holocene ice-shelf edge. This may be the case if Group A detritus, originating in an area of high shear stress, was preferentially transported at the base of the ice stream and melted out at the grounding zone, while englacial debris from other sources was transported further offshore within calved icebergs. Given the geographical restriction of Group A and its similarity to TAM Ross orogen granitoids, use of this group as a tracer in Holocene sediments may be limited. However, its potential occurrence in pre-Holocene continental rise sediments may be diagnostic for Thwaites Glacier advance to the shelf break during past glacial periods or the collapse of its drainage basin during previous interglacial periods, when an armada of icebergs may have delivered vast amounts of IRD with a Group A signature to the offshore (e.g., Bailey et al., 2022; MacAyeal, 1992).

Simões Pereira et al. (2018) did not identify a ~490 Ma signal in ice-rafted hornblende grains from nearby site PS75/168–1. The absence may be due to a bathymetric ridge which extends to the north and east of site 34MC and acted as a pinning point for Thwaites Glacier's Eastern Ice Shelf in the recent past (Clark et al., 2024). While site 34MC received IRD only from Thwaites Glacier, site PS75/168–1 on the NW side of the ridge could also receive IRD supplied by icebergs calved from Pine Island Glacier, which probably diluted the ~490 Ma Thwaites signal (possibly exacerbated by the small sample size of 9 hornblende grains from that site and/or low hornblende fertility of the ~490 Ma source, underpinning the utility of abundant feldspar as a provenance tracer).

Group B grains occur in sample 28PC (Sulzberger Bay) and sample 14PC, the next location to the west. The Pb isotopic signature of Group B is relatively coherent (Fig. 5a). An isochron constructed from Group B grains yields an age of 344 ± 32 Ma and $^{87}Sr/^{86}Sr_i$ of 0.7157 ± 0.0082 (Fig. 6b). Glaciogenic debris from the Ford Ranges (Fig. 2), discharged by glaciers flowing into Sulzberger Bay, is the most likely source of Group B feldspars. Exposures in the region comprise meta-sediments of the Neoproterozoic–Cambrian Swanson Formation, which were intruded by the Ford Granodiorite suite and anatectic granites at ~375 Ma and 358–336 Ma respectively (Korhonen et al., 2010; Yakymchuk et al., 2015). Mid-crustal equivalents of the Swanson Formation and Ford Granodiorite are migmatitic paragneisses and orthogneisses exposed in the Fosdick Mountains. Group B's isochron age matches that of the younger anatectic granite. The $^{87}Sr/^{86}Sr_i$ is significantly higher than the ~0.706–0.708 of the Ford Granodiorite but falls at the lower end of the range of values reported for the Swanson Formation (~0.712–0.735 at 350 Ma; Korhonen et al., 2010; Yakymchuk et al., 2015), suggesting the source for Group B Kfs had a component of migmatized Swanson Formation (or otherwise similarly reworked crust). Both the age and $^{87}Sr/^{86}Sr_i$ of Group B closely resemble a monzogranite (C5-Is51A) sampled at Mount Iphigene in the Ford Ranges, dated by zircon U–Pb to 353 ± 3 Ma (Siddoway and Fanning, 2009) with $^{87}Sr/^{86}Sr_{350Ma}$ = 0.7152 (Korhonen et al., 2010). This monzogranite is interpreted by Korhonen et al. (2010) as a product of anatexis of the

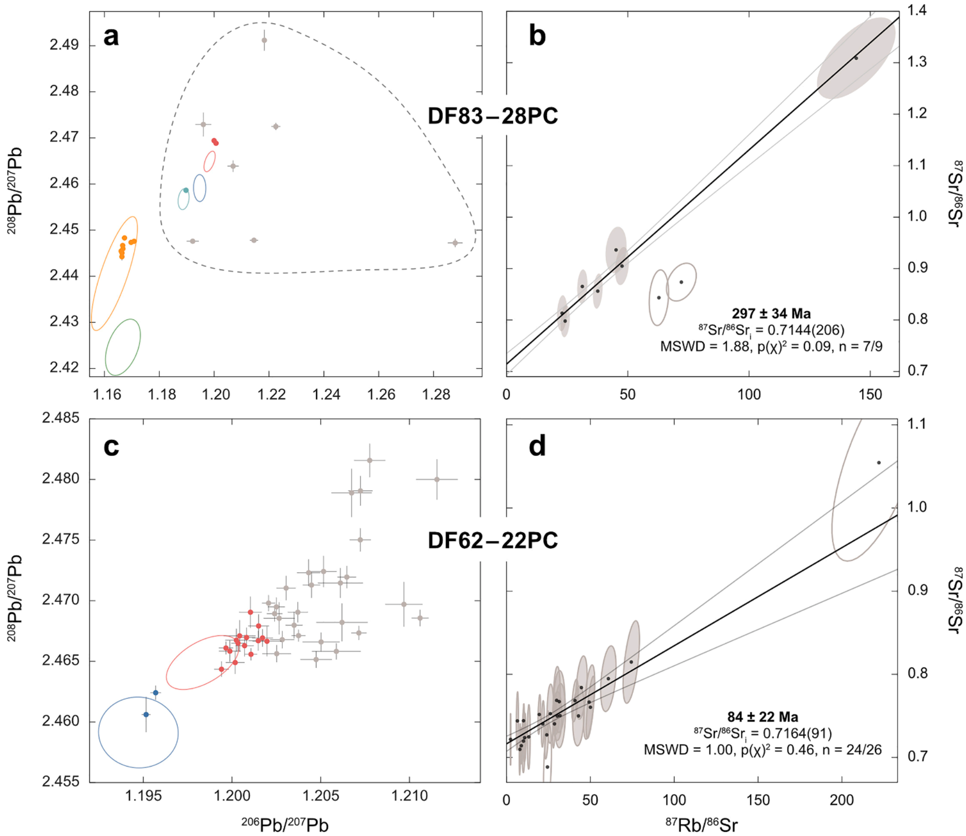

Fig. 7. Isochrons constructed from outlying Pb isotopic data in samples 28PC and 22PC. Abbreviations and isochrons are described in Fig. 6, and Pb group confidence ellipses and colours follow Fig. 5. The isochron in (b) is constructed from the grains inside the dashed line in (a); The isochron in (d) is constructed from a subset of all the grains shown in (c). Including the highest $^{87}Rb/^{86}Sr$ spot in (d) yields an age of 95 ± 18 Ma (MSWD = 1.05).

Swanson Formation. The high abundance of Group B grains (high $^{87}Sr/^{86}Sr_i$ and ~344 Ma age) in our sample 28PC points to a significant subglacial exposure of its source and may substantiate the longer duration and greater geographic extent of Devonian–Carboniferous crustal assimilation hypothesized by Yakymchuk et al. (2015).

The discovery of a connection between Group B feldspars and a proximal, well-characterized source in the Fosdick Metamorphic Complex validates our Pb–Rb–Sr method for Kfs and supports its application to much more distal sources, including those in subglacial bedrock.

55% of grains in sample 28PC are not classified as Group B, but instead mostly fall outside any of the Pb groups defined by clustering (Fig. 7a). These grains have variable Pb isotope compositions, consistent with a sedimentary origin, but a uniform Rb–Sr age suggesting high-

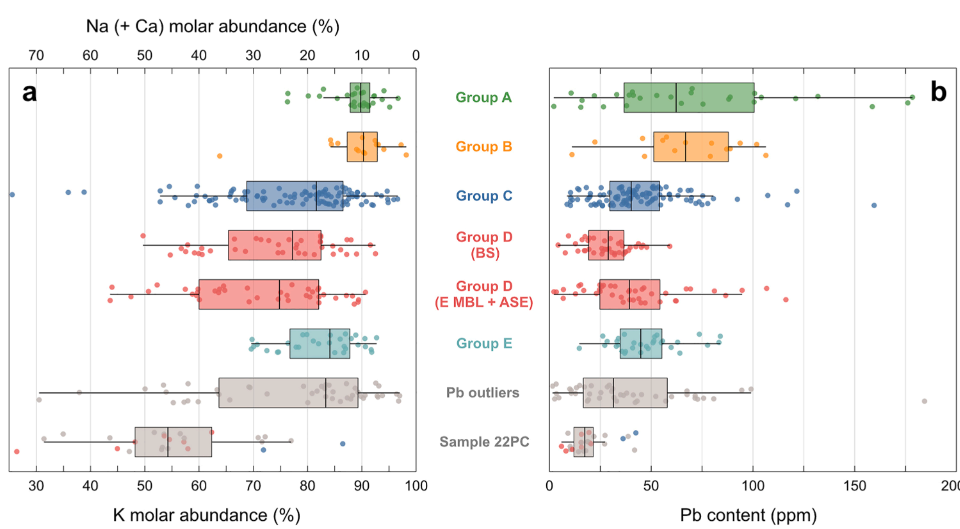

Fig. 8. Elemental composition of Kfs grains analysed in this study, presented by Pb group and for sample 22PC. **a**, Feldspar composition along the alkali feldspar solid solution, given by the molar abundance of K. A secondary axis for reference shows the molar abundance of Na with a negligible contribution from Ca (0.5% overall median of all grains). **b**, Pb abundance in parts per million (ppm). ASE: Amundsen Sea Embayment, BS: Bellingshausen Sea, E MBL: Eastern Marie Byrd Land.

grade regional metamorphic resetting. They form an isochron with an age of 297 ± 34 Ma (MSWD = 1.9, n = 7; Fig. 7b), corresponding to the shoulder at ~300 Ma visible in the regional KDE (Fig. 4b). Outcrops in western MBL do not record ~300 Ma metamorphism, so the grains may reflect an unexposed source, an unrecognized event, or deposition from icebergs drifting in the westward-flowing coastal current (Fig. 5c).

Sample 22PC at the central Ross Ice Shelf edge contains an unusually high proportion (61%) of grains not assigned to any group by clustering. These unassigned grains form a well-constrained 84 ± 22 Ma isochron (MSWD = 1.00, n = 24; Fig. 7d) and have Pb isotope compositions that form a relatively coherent but dispersed group, offset from the radiogenic end of Group D (Fig. 7c). This may be the result of low ^{207}Pb counts and associated ratio imprecision (Fig. 8b). However, high Na content (Fig. 8a) and a distinctive mottled appearance in backscattered electron images (Fig. S7) suggest that hydrothermal albitisation at ~84 Ma may have reset their age and disturbed their Pb isotopes, potentially linking them to Group D Kfs (see below). Almost all samples contain unassigned grains, but in much lower proportions (~15–30%) than in sample 22PC.

Group C forms the largest component of seven samples, from sites near the TICB. The Middle Jurassic age (171 ± 12 Ma; Fig. 6c) and relatively high Na content of the feldspar grains in this group (Fig. 8a) indicate a volcanic origin contemporaneous with the Chon Aike Silicic Large Igneous Province (Bastias et al., 2021). The age for Group C material places TICB magmatism at the very earliest part of the Chon Aike V2 phase (173–160 Ma; Bastias et al., 2021), and the $^{87}Sr/^{86}Sr_i$ of Group C (0.7062 ± 0.0022) matches that of the V2-aged Mapple Formation ($^{87}Sr/^{86}Sr_{168Ma}$ = 0.706–0.707; Riley et al., 2001). Fixing the Group C isochron to 185 Ma yields $^{87}Sr/^{86}Sr_i$ = 0.7044, excluding a correlation with the V1-aged (188–178 Ma) Mount Poster Formation ($^{87}Sr/^{86}Sr_{185Ma}$ = ~0.7106–0.7206; Riley et al., 2001).

A peak in activity within the V2 phase along the eastern ASE coastline is evident in ice-rafted hornblende and biotite grains ($^{40}Ar/^{39}Ar$ ages of ~170 Ma; Simões Pereira et al., 2018). Zircon U–Pb ages from granitoid glacial erratic boulders from Pine Island Glacier (~175 Ma; Jordan et al., 2025), the Sif Island granite (~177–174 Ma; Marschalek et al., 2024b), and sediments recovered offshore/under Pine Island and Thwaites glaciers (~175 Ma; Marschalek et al., 2025) place plutonic emplacement slightly earlier, during an apparent pause in magmatism on the Antarctic Peninsula (Bastias et al., 2021). A 182 ± 1 Ma crystal tuff at Mount Dowling (zircon U–Pb; Riley et al., 2017) indicates the presence of the Chon Aike V1 phase on Thurston Island, and the V3 phase is apparent in the dominant 152–142 Ma onshore plutons in the TICB (Rb–Sr, Pankhurst et al., 1993). On this basis, the TICB belongs in the Chon Aike province, consistent with some reconstructions (e.g., Craddock et al., 2017), but contrary to others (e.g., Bastias et al., 2021). Evidently, the ~178–173 Ma pause in magmatism (Bastias et al., 2021) was restricted to the Antarctic Peninsula.

We observe a significant presence of Group C Kfs grains in IRD deposited at site 34MC, confirming previous suggestions (Spiegel et al., 2016; Zundel et al., 2019) that the TICB boundary runs not along the Pine Island rift, but beneath Thwaites Glacier – specifically, further west than its eastern shear margin (cf. Marschalek et al., 2024b). Kfs grains at site 34MC are unlikely to have been deposited by icebergs calved from Pine Island Glacier because icebergs would have been blocked by the bathymetric ridge that separates site 34MC from Pine Island Bay.

A minor Group C signal, probably contributed by westward-drifting icebergs, appears offshore in samples from the Dotson-Getz Trough but not in samples along the MBL coast, which are likely more influenced by local inputs from MBL glaciers. A small Group C signal reappears in the eastern Ross Sea, where detrital zircon and hornblende grains under the Siple Coast ice streams share a similar Jurassic age (Licht et al., 2014; Marschalek et al., 2024a). Assuming that the Kfs grains on the Ross Sea margin are cogenetic with the rest of Group C (i.e., not just a coincidental Pb isotope signature) and that the Chon Aike province does not extend into the West Antarctic interior, their deposition there could be explained by either (i) transport via westward-drifting icebergs calved from Thwaites Glacier or further east or (ii) re-working from sedimentary rocks in the West Antarctic interior. In the former case, the Jurassic zircons may relate not to the Chon Aike Silicic Large Igneous Province, but to the contemporaneous (mafic) Ferrar Large Igneous Province (Jordan et al., 2020). However, the absence of Group C grains in the samples from the MBL coast argues against significant IRD supply via the Antarctic coastal current. The second possibility is therefore more likely: that the grains are derived from sedimentary strata deposited in the area of the Byrd Subglacial Basin before the formation of the WAIS – i.e., during the Paleogene (Klages et al., 2024). This seems plausible given a similarly aged detrital zircon population in a late Eocene fluvial sandstone present on the eastern Amundsen Sea shelf (Marschalek et al., 2025) and possibly extending well into the West Antarctic interior (Zundel et al., 2019). The absence of the Group C signal in samples from around Alexander Island may be due to the influence of sediment sourcing or routing from this island, which is part of the geologically distinct 'Western Domain' identified in the Antarctic Peninsula terrane model (Vaughan and Storey, 2000) and which does not provide a source for ~170 Ma Kfs grains.

Group D is the largest component in nearly half of our samples, especially along the coasts of eastern MBL (Getz Ice Shelf) and the Antarctic Peninsula. Age data derived from all Group D grains are overdispersed, but splitting the group into geographical sub-groups yields isochrons of 113 ± 23 Ma for Group D in eastern MBL and the ASE, and 84 ± 39 Ma in the Bellingshausen Sea (Fig. 6). These mid-late Cretaceous ages coincide with widespread magmatism (Riley et al., 2018) associated with intracontinental extension (Jordan et al., 2020; Luyendyk, 1995; Siddoway et al., 2004) and eventual breakup (Mortimer et al., 2019) of East Gondwana. Our Pb isotope data show subtle differences within Group D between samples from the ASE and Bellingshausen Sea (see Fig. S8), likely reflecting differing contributions of crustal melts developed in terranes with different geological characteristics during discontinuous magmatism (Jordan et al., 2020; Riley et al., 2018).

The Rb–Sr age of Group D in the Bellingshausen Sea resembles that of Group E (91 ± 35 Ma; Fig. 6e), and the $^{87}Sr/^{86}Sr_i$ values are also within uncertainty of each other (Fig. 6f). However, the $^{87}Sr/^{86}Sr_i$ of Group E is elevated, indicating a higher crustal contribution. Group E grains are more K-rich on average (Fig. 8a) but have Pb isotope compositions that are less radiogenic (Fig. 5a) and clearly separated from those of Group D.

Groups C, D (both subgroups), E and unassigned grains of sample 22PC appear to reflect ~170 Ma, ~110 Ma, and ~85 Ma peak magmatic activity along the Gondwana margin (Riley et al., 2018). Repeated magmatic flare-ups occurring every ~25–50 Myr are typical of continental margin arcs (DeCelles et al., 2009). Variation between these Pb groups is likely a response to the degree and type of crustal assimilation from varied source rocks and different lithospheric mantle composition and slab components, reflecting Mesozoic oblique convergence between the Phoenix oceanic and Gondwana continental plates (Jordan et al., 2020) along with inheritance of along-arc isotopic variations acquired in the late Paleozoic (Nelson and Cottle, 2018).

4.1. Methodological considerations

Initial $^{87}Sr/^{86}Sr$ for our Pb isotope groups ranges from 0.7062 ± 0.0022 to 0.7157 ± 0.0082 (Fig. 6f). Consequently, some group isochron ages (without $^{87}Sr/^{86}Sr_i$ assumptions) differ slightly from peaks in the detrital spectra (Fig. S6) (e.g., Group B detrital peak ≈ 360 Ma; isochron = 344 ± 32 Ma). These discrepancies suggest that using a weighted mean to estimate detrital Kfs $^{87}Sr/^{86}Sr_i$ is not ideal, in contrast to biotite where the higher $^{87}Rb/^{86}Sr$ reduces the effect of $^{87}Sr/^{86}Sr_i$ variation (Rösel and Zack, 2022). The single-grain age data should therefore be interpreted with caution, and since the isochron ages fall within the detrital peaks and use all Rb–Sr data without $^{87}Sr/^{86}Sr_i$ assumptions, the isochrons represent our preferred ages.

The clustering algorithms used here are not capable of weighting by uncertainty. Where uncertainty is low, this is a reasonable simplification, as demonstrated by the independent Rb–Sr age verification of our Pb compositional clusters. Ignoring large analytical uncertainties, however, could lead to clustering errors. In the absence of more precise Pb isotope data (potentially achievable by using 10^{13} Ω amplifier or ion-counting detector technology), we therefore recommend using ^{207}Pb-normalization for clustering. However, reducing analytical uncertainty or including uncertainty weighting in clustering algorithms are both possible. The development of multi-collector ICP–MS/MS methods for in situ Rb–Sr dating should allow single-grain detrital Kfs dating at much better precision than the triple-quadrupole method used here, especially at low $^{87}Rb/^{86}Sr$ (Fig. 15 in Bevan et al., 2021), mitigating the currently unavoidable bias towards high $^{87}Rb/^{86}Sr$ grains and permitting the geochronological data to be included in clustering algorithms (although accuracy would still be controlled by how $^{87}Sr/^{86}Sr_i$ is determined). Refinement of the triple-quadrupole ICP–MS/MS method by improving availability of suitable feldspar reference materials with precise reference ages may also reduce propagated single-grain age uncertainties sufficiently to permit their inclusion in the clustering process.

5. Conclusions

Coupled Pb isotope analysis and Rb–Sr dating of detrital feldspars represent a viable and useful approach for characterizing bedrock concealed by ice sheets and establishing the provenance of ice-rafted marine sediments. Gaussian mixture modelling, when outliers are managed with density-based clustering, resolves fine-scale variability in the Pb isotopic composition of West Antarctic Kfs grains and reveals geographically distinct Pb isotope clusters, each associated with distinct and well-constrained Rb–Sr isochron ages. Material with a unique Pb-isotope signature and Carboniferous Rb–Sr age in a sediment sample from Sulzberger Bay matches closely with the local onshore geology of the Ford Ranges, validating the approach and its extension to less well-characterized areas.

Isotopically and geochronologically distinct Kfs grains are supplied to the termini of both Thwaites Glacier and the eastern Ross Ice Shelf by a subglacial felsic body, inferred to match the granitoids beneath the WAIS divide recently described from aerogeophysical observations. The ~490 Ma age of these grains indicates the source is probably an outcrop of Ross orogen granitoids within a rifted micro-block of the TAM. Middle Jurassic–aged Kfs grains with another distinct Pb isotope signature are sourced from the TICB and correlate with the V2 phase of the Chon Aike Silicic Large Igneous Province. The abundance of these grains in detritus shed by Thwaites Glacier confirms that the MBL/TICB boundary runs beneath it.

In situ Pb isotopic compositions of ice-rafted feldspars can be added to the West Antarctic IRD provenance toolbox and, especially when coupled with in situ Rb–Sr dating, can be used to address other inverse provenance challenges in different geological contexts. Ice-rafted Kfs grains are suitable tracers for reconstructing past ice-sheet extent and erosional dynamics in the Amundsen Sea sector.

CRediT authorship contribution statement

Thomas Arney: Writing – review & editing, Writing – original draft, Visualization, Validation, Software, Methodology, Investigation, Formal analysis, Data curation, Conceptualization. **Claus-Dieter Hillenbrand:** Writing – review & editing, Supervision, Resources, Project administration, Methodology, Funding acquisition, Formal analysis, Conceptualization. **Thomas M. Belgrano:** Writing – review & editing, Validation, Resources, Methodology, Formal analysis, Conceptualization. **J. Andy Milton:** Writing – review & editing, Validation, Project administration, Methodology, Investigation. **Christine S. Siddoway:** Writing – review & editing, Resources, Formal analysis. **Gavin L. Foster:** Writing – review & editing, Supervision, Funding acquisition, Conceptualization. **Paul A. Wilson:** Writing – review & editing, Supervision, Project administration, Methodology, Funding acquisition, Conceptualization. **Julia S. Wellner:** Writing – review & editing, Resources. **Steve M. Bohaty:** Writing – review & editing, Supervision, Project administration, Methodology, Funding acquisition, Formal analysis, Conceptualization.

Declaration of competing interest

The authors declare that they have no known competing financial interests or personal relationships that could have appeared to influence the work reported in this paper.

Acknowledgements

We thank Rex Taylor, Keiji Horikawa, Ian Bailey, and Teal Riley for useful discussions; Miros Charidemou and Val Stanley for help with sampling; Dan Doran, Matt Beverley-Smith, and Richard Pearce for their help in preparing and imaging samples; Carlos Corella Santa Cruz and Kerstin Drost for K-feldspar samples and preliminary age information; Tereza Kunkelova for comments on an early version of the manuscript; and the captains, officers, crews, and science parties of RVIB *Nathaniel B. Palmer* expedition NBP2002 and RRS *James Clark Ross* expeditions JR104, JR141, and JR179. We are also grateful to the editors and to Michael Flowerdew and another anonymous reviewer whose comments and suggestions helped improve this article.

The British Antarctic Survey and the British Ocean Sediment Core Research Facility (BOSCORF) are thanked for supplying sediment samples. Samples were also provided by the Marine and Geology Repository, Oregon State University (OSU-MGR). This work used samples from the THOR project, a component of the International Thwaites Glacier Collaboration (ITGC), with support from National Science Foundation (NSF: grant 1738942) and Natural Environment Research Council (NERC: grant nos. NE/S006664/1, and NE/S006672/1). This work was supported by NERC grant number NE/S007210/1. CSS was supported by the NSF (grant 1917176), including some of the sampling at OSU-MGR. TMB acknowledges funding under Geological Survey Ireland Grant Agreement 2023-TgC-025 (Project ElRbSr).

Supplementary materials

Supplementary material associated with this article can be found, in the online version, at doi:10.1016/j.epsl.2026.120298.

Data availability

All processing code used here is archived with Zenodo (https://doi.org/10.5281/zenodo.21496573). All supporting data have been permanently deposited and are freely accessible at the UK Polar Data Centre (https://doi.org/10.5285/e785832b-6dc6-4dba-aeb4-4fcdbf6716f0).

References

Adams, C.J., 1986. Geochronological studies of the Swanson Formation of Marie Byrd Land, West Antarctica, and correlation with northern Victoria Land, East Antarctica, and South Island, New Zealand. N. Z. J. Geol. Geophys. 29, 345–358. https://doi.org/10.1080/00288306.1986.10422157.

Adams, C.J., Bradshaw, J.D., Ireland, T.R., 2014. Provenance connections between late Neoproterozoic and early Palaeozoic sedimentary basins of the Ross Sea region, Antarctica, south-east Australia and southern Zealandia. Antarct. Sci. 26, 173–182. https://doi.org/10.1017/S0954102013000461.

Ankerst, M., Breunig, M.M., Kriegel, H.-P., Sander, J., 1999. OPTICS: ordering points to identify the clustering structure. SIGMOD. Rec. 28, 49–60. https://doi.org/10.1145/304181.304187.

Arndt, J.E., Schenke, H.W., Jakobsson, M., Nitsche, F.O., Buys, G., Goleby, B., Rebesco, M., Bohoyo, F., Hong, J., Black, J., Greku, R., Udintsev, G., Barrios, F., Reynoso-Peralta, W., Taisei, M., Wigley, R., 2013. The International Bathymetric Chart of the Southern Ocean (IBCSO) Version 1.0—A new bathymetric compilation covering circum-Antarctic waters. Geophys. Res. Lett. 40, 3111–3117. https://doi.org/10.1002/grl.50413.

Bailey, I., Hemming, S., Reilly, B.T., Rollinson, G., Williams, T., Weber, M.E., Raymo, M. E., Peck, V.L., Ronge, T.A., Brachfeld, S., O'Connell, S., Tauxe, L., Warnock, J.P., Armbrecht, L., Cardillo, F.G., Du, Z., Fauth, G., Garcia, M., Glueder, A., Guitard, M., Gutjahr, M., Hernández-Almeida, I., Hoem, F.S., Hwang, J.-H., Iizuka, M., Kato, Y., Kenlee, B., Martos, Y.M., Pérez, L.F., Seki, O., Tripathi, S., Zheng, X., 2022. Episodes of Early Pleistocene West Antarctic ice sheet retreat recorded by Iceberg Alley sediments. Paleoceanogr. Paleoclimatol. 37, e2022PA004433. https://doi.org/10.1029/2022PA004433.

Bastias, J., Spikings, R., Riley, T., Ulianov, A., Grunow, A., Chiaradia, M., Hervé, F., 2021. A revised interpretation of the Chon Aike magmatic province: active margin origin and implications for the opening of the Weddell Sea. Lithos 386-387, 106013. https://doi.org/10.1016/j.lithos.2021.106013.

Bevan, D., Coath, C.D., Lewis, J., Schwieters, J., Lloyd, N., Craig, G., Wehrs, H., Elliott, T., 2021. In Situ Rb–Sr dating by collision cell, multicollection inductively-coupled plasma mass-spectrometry with pre-cell mass-filter, (CC-MC-ICPMS/MS). J. Anal. Spectrom. 36, 917–931. https://doi.org/10.1039/D1JA00006C.

Bingham, R.G., Siegert, M.J., 2009. Quantifying subglacial bed roughness in Antarctica: implications for ice-sheet dynamics and history. Quat. Sci. Rev. 28, 223–236. https://doi.org/10.1016/j.quascirev.2008.10.014, 223–236.

Clark, R.W., Wellner, J.S., Hillenbrand, C.-D., Totten, R.L., Smith, J.A., Miller, L.E., Larter, R.D., Hogan, K.A., Graham, A.G.C., Nitsche, F.O., Lehrmann, A.A., Lepp, A.P., Kirkham, J.D., Fitzgerald, V.T., Garcia-Barrera, G., Ehrmann, W., Wacker, L., 2024. Synchronous retreat of Thwaites and Pine Island glaciers in response to external forcings in the presatellite era. Proc. Natl. Acad. Sci. USA 121, e2211711120. https://doi.org/10.1073/pnas.2211711120.

Cox, S.C., Smith Lyttle, B., Elkind, S., Siddoway, C.S., Morin, P., Capponi, G., Abu-Alam, T., Ballinger, M., Bamber, L., Kitchener, B., Lelli, L., Mawson, J.F., Millikin, A., Dal Seno, N., Whitburn, L., White, T., Burton-Johnson, A., Crispini, L., Elliot, D., Elvevold, S., Goodge, J.W., Halpin, J.A., Jacobs, J., Mikhalsky, E., Martin, A.P., Morgan, F., Smellie, J., Scadden, P., Wilson, G.S., 2023. The GeoMAP (v.2022-08) continent-wide detailed geological dataset of Antarctica. https://doi.org/10.1594/PANGAEA.951482.

Craddock, J.P., Schmitz, M.D., Crowley, J.L., Larocque, J., Pankhurst, R.J., Juda, N., Konstantinou, A., Storey, B., 2017. Precise U-Pb zircon ages and geochemistry of Jurassic granites, Ellsworth-Whitmore terrane, central Antarctica. GSA Bull. 129, 118–136. https://doi.org/10.1130/B31485.1.

Cribb, S.J., 1975. Rubidium–strontium ages and strontium isotope ratios from the igneous rocks of Leicestershire. J. Geol. Soc. Lond. 131, 203–212. https://doi.org/10.1144/gsjgs.131.2.0203.

Darbyshire, D.P.F., Shepherd, T.J., 1985. Chronology of granite magmatism and associated mineralization, SW England. J. Geol. Soc. Lond. 142, 1159–1177. https://doi.org/10.1144/gsjgs.142.6.1159.

de Laeter, J.R., Böhlke, J.K., de Bièvre, P., Hidaka, H., Peiser, H.S., Rosman, K.J.R., Taylor, P.D.P., 2003. Atomic weights of the elements. review 2000 (IUPAC technical report). Pure Appl. Chem. 75, 683–800. https://doi.org/10.1351/pac200375060683.

DeCelles, P.G., Ducea, M.N., Kapp, P., Zandt, G., 2009. Cyclicity in cordilleran orogenic systems. Nat. Geosci. 2, 251–257. https://doi.org/10.1038/ngeo469.

Demartis, M., Jung, S., Hauff, F., Aragón, E., D'Eramo, F.J., Coniglio, J.E., Pinotti, L.P., Boffadossi, M.A., Muratori, M.E., Coniglio, J., 2021. Shear-assisted water-fluxed melting and AFC processes in the foreland of the early Paleozoic famatinian orogen: petrogenesis of leucogranites and pegmatites from the Sierras de Córdoba, Argentina. Int. J. Earth. Sci. 110, 2495–2517. https://doi.org/10.1007/s00531-020-01961-2.

Ehrmann, W., Hillenbrand, C.-D., Smith, J.A., Graham, A.G.C., Kuhn, G., Larter, R.D., 2011. Provenance changes between recent and glacial-time sediments in the Amundsen Sea embayment, West Antarctica: clay mineral assemblage evidence. Antarct. Sci. 23, 471–486. https://doi.org/10.1017/S0954102011000320.

Flowerdew, M.J., Tyrrell, S., Boger, S.D., Fitzsimons, I.C.W., Harley, S.L., Mikhalsky, E. V., Vaughan, A.P.M., 2013a. Pb isotopic domains from the Indian Ocean sector of Antarctica: implications for past Antarctica–India connections. Antarctica and Supercontinent Evolution. Geological Society, London, Special Publications, London, pp. 59–72. https://doi.org/10.1144/SP383.3.

Flowerdew, M.J., Tyrrell, S., Peck, V.L., 2013b. Inferring sites of subglacial erosion using the Pb isotopic composition of ice-rafted feldspar: examples from the Weddell Sea. Geology 41, 147–150. https://doi.org/10.1130/G33644.1.

Flowerdew, M.J., Tyrrell, S., Riley, T.R., Whitehouse, M.J., Mulvaney, R., Leat, P.T., Marschall, H.R., 2012. Distinguishing East and West Antarctic sediment sources using the Pb isotope composition of detrital K-feldspar. Chem. Geol. 292-293, 88–102. https://doi.org/10.1016/j.chemgeo.2011.11.006.

Gibson, D., McCormick, A.G., Meighan, I.G., Halliday, A.N., 1987. The British Tertiary Igneous Province: young Rb-Sr ages for the Mourne Mountains granites. Scott. J. Geol. 23, 221–225. https://doi.org/10.1144/sjg23020221.

Glen, R.A., Cooper, R.A., 2021. Evolution of the East Gondwana convergent margin in Antarctica, southern Australia and New Zealand from the Neoproterozoic to latest Devonian. Earth-Sci. Rev. 220, 103687. https://doi.org/10.1016/j.earscirev.2021.103687.

Glorie, S., Gilbert, S.E., Hand, M., Lloyd, J.C., 2024. Calibration methods for laser ablation Rb–Sr geochronology: comparisons and recommendation based on NIST glass and natural reference materials. Geochronology 6, 21–36. https://doi.org/10.5194/gchron-6-21-2024.

González, P.D., Sato, A.M., Naipauer, M., Varela, R., Basei, M., Sato, K., Llambías, E.J., Chemale, F., Dorado, A.C., 2018. Patagonia-Antarctica early paleozoic conjugate margins: Cambrian synsedimentary silicic magmatism, U-Pb dating of K-bentonites, and related volcanogenic rocks. Gondwana Res. 63, 186–225. https://doi.org/10.1016/j.gr.2018.05.015.

Goodge, J.W., Fanning, C.M., Fisher, C.M., Vervoort, J.D., 2024. Crustal architecture of the paleo-Pacific rift margin of East Antarctica: evidence from U-Pb ages and O-Hf isotope compositions of Ross Orogen granitoids. Geochem. Geophys. Geosyst. 25, e2024GC011435. https://doi.org/10.1029/2024GC011435.

Goodge, J.W., Fanning, C.M., Norman, M.D., Bennett, V.C., 2012. Temporal, isotopic and spatial relations of early Paleozoic Gondwana-margin arc magmatism, central Transantarctic Mountains, Antarctica. J. Petrol. 53, 2027–2065. https://doi.org/10.1093/petrology/egs043.

Halberstadt, A.R.W., Gasson, E., Pollard, D., Marschalek, J., DeConto, R.M., 2024. Geologically constrained 2-million-year-long simulations of Antarctic Ice Sheet retreat and expansion through the Pliocene. Nat. Commun. 15, 7014. https://doi.org/10.1038/s41467-024-51205-z.

Hogmalm, K.J., Zack, T., Karlsson, A.K.-O., Sjöqvist, A.S.L., Garbe-Schönberg, D., 2017. In situ Rb–Sr and K–Ca dating by LA-ICP-MS/MS: an evaluation of N_2O and SF_6 as reaction gases. J. Anal. Spectrom. 32, 305–313. https://doi.org/10.1039/C6JA00362A.

Jordan, T.A., Johnson, J.S., Riley, T.R., Conrad, E., Carter, A., 2025. Subglacial geology and palaeo flow of Pine Island Glacier from combining glacial erratics with geophysics. Commun. Earth. Environ. 6, 826. https://doi.org/10.1038/s43247-025-02783-3.

Jordan, T.A., Riley, T.R., Siddoway, C.S., 2020. The geological history and evolution of West Antarctica. Nat. Rev. Earth. Environ. 1, 117–133. https://doi.org/10.1038/s43017-019-0013-6.

Jordan, T.A., Thompson, S., Kulessa, B., Ferraccioli, F., 2023. Geological sketch map and implications for ice flow of Thwaites Glacier, West Antarctica, from integrated aerogeophysical observations. Sci. Adv. 9, eadf2639. https://doi.org/10.1126/sciadv.adf2639.

Klages, J.P., Hillenbrand, C.-D., Bohaty, S.M., Salzmann, U., Bickert, T., Lohmann, G., Knahl, H.S., Gierz, P., Niu, L., Titschack, J., Kuhn, G., Frederichs, T., Müller, J., Bauersachs, T., Larter, R.D., Hochmuth, K., Ehrmann, W., Nehrke, G., Rodríguez-Tovar, F.J., Schmiedl, G., Spezzaferri, S., Läufer, A., Lisker, F., van de Flierdt, T., Eisenhauer, A., Uenzelmann-Neben, G., Esper, O., Smith, J.A., Pälike, H., Spiegel, C., Dziadek, R., Ronge, T.A., Freudenthal, T., Gohl, K., 2024. Ice sheet–free West Antarctica during peak early Oligocene glaciation. Science 385, 322–327. https://doi.org/10.1126/science.adj3931.

Korhonen, F.J., Saito, S., Brown, M., Siddoway, C.S., Day, J.M.D., 2010. Multiple generations of granite in the Fosdick Mountains, Marie Byrd Land, West Antarctica: implications for polyphase intracrustal differentiation in a continental margin setting. J. Petrol. 51, 627–670. https://doi.org/10.1093/petrology/egp093.

Larter, R.D., Anderson, J.B., Graham, A.G.C., Gohl, K., Hillenbrand, C.-D., Jakobsson, M., Johnson, J.S., Kuhn, G., Nitsche, F.O., Smith, J.A., Witus, A.E., Bentley, M.J., Dowdeswell, J.A., Ehrmann, W., Klages, J.P., Lindow, J., Ó Cofaigh, C., Spiegel, C., 2014. Reconstruction of changes in the Amundsen Sea and Bellingshausen Sea sector of the West Antarctic Ice Sheet since the Last Glacial Maximum. Quat. Sci. Rev. 100, 55–86. https://doi.org/10.1016/j.quascirev.2013.10.016.

Licht, K.J., Hennessy, A.J., Welke, B.M., 2014. The U-Pb detrital zircon signature of West Antarctic ice stream tills in the Ross embayment, with implications for Last Glacial Maximum ice flow reconstructions. Antarct. Sci. 26, 687–697. https://doi.org/10.1017/S0954102014000315.

Lindow, J., Kamp, P.J.J., Mukasa, S.B., Kleber, M., Lisker, F., Gohl, K., Kuhn, G., Spiegel, C., 2016. Exhumation history along the eastern Amundsen Sea coast, West Antarctica, revealed by low-temperature thermochronology. Tectonics 35, 2239–2257. https://doi.org/10.1002/2016TC004236.

Luyendyk, B.P., 1995. Hypothesis for Cretaceous rifting of east Gondwana caused by subducted slab capture. Geology 23, 373. https://doi.org/10.1130/0091-7613(1995)023<0373:HFCROE>2.3.CO;2.

MacAyeal, D.R., 1992. Irregular oscillations of the West Antarctic Ice Sheet. Nature 359, 29–32. https://doi.org/10.1038/359029a0.

Marschalek, J.W., Blard, P.-H., Sarigulyan, E., Ehrmann, W., Hemming, S.R., Thomson, S. N., Hillenbrand, C.-D., Licht, K., Tison, J.-L., Ardoin, L., Fripiat, F., Allen, C.S., Marrocchi, Y., Siegert, M.J., van de Flierdt, T., 2024a. Byrd ice core debris constrains the sediment provenance signature of central West Antarctica. Geophys. Res. Lett. 51, e2023GL106958. https://doi.org/10.1029/2023GL106958.

Marschalek, J.W., Thomson, S.N., Hillenbrand, C.-D., Vermeesch, P., Siddoway, C.S., Carter, A., Nichols, K., Rood, D.H., Venturelli, R.A., Hammond, S.J., Wellner, J., van de Flierdt, T., 2024b. Geological insights from the newly discovered granite of Sif Island between Thwaites and Pine Island glaciers. Antarct. Sci. 36, 51–74. https://doi.org/10.1017/S0954102023000287.

Marschalek, J.W., van de Flierdt, T., Siddoway, C.S., Thomson, S.N., Paxman, G.J.G., Jamieson, S.S.R., Conrad, E., Licht, K.J., Hemming, S.R., Bentley, M.J., Hillenbrand, C.-D., Smith, J.A., Klages, J.P., Fox, M., Pastore, G., Vermeesch, P., 2025. Reconstructing Eocene Antarctic river drainage from provenance analysis of Amundsen Sea Embayment sediments. Sci. Adv. 11, eaea2373. https://doi.org/10.1126/sciadv.aea2373.

Mortimer, N., van den Bogaard, P., Hoernle, K., Timm, C., Gans, P.B., Werner, R., Riefstahl, F., 2019. Late Cretaceous oceanic plate reorganization and the breakup of Zealandia and Gondwana. Gondwana Res. 65, 31–42. https://doi.org/10.1016/j.gr.2018.07.010.

Mouginot, J., Scheuchl, B., Rignot, E., 2017. MEaSUREs annual Antarctic ice velocity maps, 2006-2017, version 1. https://doi.org/10.5067/9T4EPQXTJYW9.

Mulder, J.A., Halpin, J.A., Daczko, N.R., Orth, K., Meffre, S., Thompson, J.M., Morrissey, L.J., 2019. A multiproxy provenance approach to uncovering the assembly of east Gondwana in Antarctica. Geology 47, 645–649. https://doi.org/10.1130/G45952.1.

Nelson, D.A., Cottle, J.M., 2018. The secular development of accretionary orogens: linking the Gondwana magmatic arc record of West Antarctica, Australia and South America. Gondwana Res. 63, 15–33. https://doi.org/10.1016/j.gr.2018.06.002.

Neofitu, R., Mark, C., O'Connell, S., Zack, T., Rösel, D., Mark, D., Barfod, D., Flowerdew, M.J., Kelley, S., Daly, J.S., 2024. Dynamic collapse and regrowth of the Antarctic Ice Sheet in the Weddell Sea sector during the middle Miocene: a novel multi-proxy sedimentary provenance approach using *in-situ* ^{87}Rb/^{87}Sr dating of detrital K-feldspar. Earth. Planet. Sci. Lett. 641, 118824. https://doi.org/10.1016/j.epsl.2024.118824.

Noble, S.R., Tucker, R.D., Pharaoh, T.C., 1993. Lower Palaeozoic and Precambrian igneous rocks from eastern England, and their bearing on late Ordovician closure of the Tornquist Sea: constraints from U-Pb and Nd isotopes. Geol. Mag. 130, 835–846. https://doi.org/10.1017/S0016756800023190.

Pankhurst, R.J., Millar, I.L., Grunow, A.M., Storey, B.C., 1993. The pre-Cenozoic magmatic history of the Thurston Island Crustal Block, West Antarctica. J. Geophys. Res.: Solid Earth 98, 11835–11849. https://doi.org/10.1029/93JB01157.

Pankhurst, R.J., Weaver, S.D., Bradshaw, J.D., Storey, B.C., Ireland, T.R., 1998. Geochronology and geochemistry of pre-Jurassic superterranes in Marie Byrd Land, Antarctica. J. Geophys. Res.: Solid Earth 103, 2529–2547. https://doi.org/10.1029/97JB02605.

Paton, C., Hellstrom, J., Paul, B., Woodhead, J., Hergt, J., 2011. Iolite: freeware for the visualisation and processing of mass spectrometric data. J. Anal. Spectrom. 26, 2508. https://doi.org/10.1039/C1JA10172B.

Rackow, T., Wesche, C., Timmermann, R., Hellmer, H.H., Juricke, S., Jung, T., 2017. A simulation of small to giant Antarctic iceberg evolution: differential impact on climatology estimates. J. Geophys. Res.: Oceans 122, 3170–3190. https://doi.org/10.1002/2016JC012513.

Rapela, C.W., Pankhurst, R.J., Casquet, C., Dahlquist, J.A., Mark Fanning, C., Baldo, E.G., Galindo, C., Alasino, P.H., Ramacciotti, C.D., Verdecchia, S.O., Murra, J.A., Basei, M.A.S., 2018. A review of the Famatinian Ordovician magmatism in southern South America: evidence of lithosphere reworking and continental subduction in the early proto-Andean margin of Gondwana. Earth-Sci. Rev. 187, 259–285. https://doi.org/10.1016/j.earscirev.2018.10.006.

Redaa, A., Farkaš, J., Gilbert, S., Collins, A.S., Wade, B., Löhr, S., Zack, T., Garbe-Schönberg, D., 2021. Assessment of elemental fractionation and matrix effects during in situ Rb–Sr dating of phlogopite by LA-ICP-MS/MS: implications for the accuracy and precision of mineral ages. J. Anal. Spectrom. 36, 322–344. https://doi.org/10.1039/D0JA00299B.

Riley, T.R., Burton-Johnson, A., Flowerdew, M.J., Poblete, F., Castillo, P., Hervé, F., Leat, P.T., Millar, I.L., Bastias, J., Whitehouse, M.J., 2023. Palaeozoic – Early Mesozoic geological history of the Antarctic Peninsula and correlations with Patagonia: kinematic reconstructions of the proto-Pacific margin of Gondwana. Earth-Sci. Rev. 236, 104265. https://doi.org/10.1016/j.earscirev.2022.104265.

Riley, T.R., Burton-Johnson, A., Flowerdew, M.J., Whitehouse, M.J., 2018. Episodicity within a mid-Cretaceous magmatic flare-up in West Antarctica: U-Pb ages of the Lassiter Coast intrusive suite, Antarctic Peninsula, and correlations along the Gondwana margin. GSA Bull. 130, 1177–1196. https://doi.org/10.1130/B31800.1.

Riley, T.R., Flowerdew, M.J., Pankhurst, R.J., Leat, P.T., Millar, I.L., Fanning, C.M., Whitehouse, M.J., 2017. A revised geochronology of Thurston Island, West Antarctica, and correlations along the proto-pacific margin of Gondwana. Antarct. Sci. 29, 47–60. https://doi.org/10.1017/S0954102016000341.

Riley, T.R., Leat, P.T., Pankhurst, R.J., Harris, C., 2001. Origins of large volume rhyolitic volcanism in the Antarctic Peninsula and Patagonia by crustal melting. J. Petrol. 42, 1043–1065. https://doi.org/10.1093/petrology/42.6.1043.

Rösel, D., Zack, T., 2022. LA-ICP-MS/MS single-spot Rb-Sr dating. Geostand. Geoanalytical Res. 46, 143–168. https://doi.org/10.1111/ggr.12414.

Siddoway, C.S., Baldwin, S.L., Fitzgerald, P.G., Fanning, C.M., Luyendyk, B.P., 2004. Ross Sea mylonites and the timing of intracontinental extension within the West Antarctic rift system. Geology 32, 57. https://doi.org/10.1130/G20005.1.

Siddoway, C.S., Fanning, C.M., 2009. Paleozoic tectonism on the East Gondwana margin: evidence from SHRIMP U–Pb zircon geochronology of a migmatite–granite complex in West Antarctica. Tectonophysics 477, 262–277. https://doi.org/10.1016/j.tecto.2009.04.021.

Simões Pereira, P., van de Flierdt, T., Hemming, S.R., Hammond, S.J., Kuhn, G., Brachfeld, S., Doherty, C., Hillenbrand, C.-D., 2018. Geochemical fingerprints of glacially eroded bedrock from West Antarctica: detrital thermochronology, radiogenic isotope systematics and trace element geochemistry in Late Holocene glacial-marine sediments. Earth-Sci. Rev. 182, 204–232. https://doi.org/10.1016/j.earscirev.2018.04.011.

Spiegel, C., Lindow, J., Kamp, P.J.J., Meisel, O., Mukasa, S., Lisker, F., Kuhn, G., Gohl, K., 2016. Tectonomorphic evolution of Marie Byrd Land – Implications for cenozoic rifting activity and onset of West Antarctic glaciation. Glob. Planet. Change. 145, 98–115. https://doi.org/10.1016/j.gloplacha.2016.08.013.

Stacey, J.S., Kramers, J.D., 1975. Approximation of terrestrial lead isotope evolution by a two-stage model. Earth. Planet. Sci. Lett. 26, 207–221. https://doi.org/10.1016/0012-821X(75)90088-6.

Tankersley, M.D., Horgan, H.J., Siddoway, C.S., Caratori Tontini, F., Tinto, K.J., 2022. Basement topography and sediment thickness beneath Antarctica's Ross Ice Shelf. Geophys. Res. Lett. 49, e2021GL097371. https://doi.org/10.1029/2021GL097371.

Tyrrell, S., Haughton, P.D.W., Daly, J.S., Kokfelt, T.F., Gagnevin, D., 2006. The use of the common Pb isotope composition of detrital K-feldspar grains as a provenance tool and its application to Upper Carboniferous paleodrainage, northern England. J. Sediment. Res. 76, 324–345. https://doi.org/10.2110/jsr.2006.023.

Vaughan, A.P.M., Storey, B.C., 2000. The eastern Palmer Land shear zone: A new terrane accretion model for the Mesozoic development of the Antarctic Peninsula. J. Geol. Soc. Lond. 157, 1243–1256. https://doi.org/10.1144/jgs.157.6.1243.

Vermeesch, P., 2018. IsoplotR: a free and open toolbox for geochronology. Geosci. Front. 9, 1479–1493. https://doi.org/10.1016/j.gsf.2018.04.001.

Williams, T., van de Flierdt, T., Hemming, S.R., Chung, E., Roy, M., Goldstein, S.L., 2010. Evidence for iceberg armadas from East Antarctica in the Southern Ocean during the late Miocene and early Pliocene. Earth. Planet. Sci. Lett. 290, 351–361. https://doi.org/10.1016/j.epsl.2009.12.031.

Yakymchuk, C., Brown, C.R., Brown, M., Siddoway, C.S., Fanning, C.M., Korhonen, F.J., 2015. Paleozoic evolution of western Marie Byrd Land, Antarctica. GSA Bull. 127, 1464–1484. https://doi.org/10.1130/B31136.1.

Zundel, M., Spiegel, C., Mehling, A., Lisker, F., Hillenbrand, C.-D., Monien, P., Klügel, A., 2019. Thurston Island (West Antarctica) between Gondwana subduction and continental separation: a multistage evolution revealed by apatite thermochronology. Tectonics 38, 878–897. https://doi.org/10.1029/2018TC005150.